Materials Science and Engineering A 527 (2010) 2515–2526

Contents lists available at ScienceDirect

Materials Science and Engineering A

journal homepage: www.elsevier.com/locate/msea

Experimental characterization and modeling of the hardening behavior of the sheet steel LH800

M. Noman[a,*], T. Clausmeyer[a], C. Barthel[a], B. Svendsen[a], J. Huétink[b], M. van Riel[b]

[a] Institute of Mechanics, Dortmund University of Technology, 44227 Dortmund, Germany
[b] Netherlands Institute for Metals Research, University of Twente, 7500 AE Enschede, The Netherlands

ARTICLE INFO

Article history:
Received 26 May 2009
Received in revised form 7 December 2009
Accepted 8 December 2009

Keywords:
Material modeling
Cross hardening
Induced flow anisotropy
Metal forming
Parameter identification

ABSTRACT

In complex forming processes, sheet metal undergoes large plastic deformations involving significant induced flow anisotropy resulting from the development of persistent oriented (planar) dislocation structures. The aim of the present work is the formulation and identification of a phenomenological model which accounts for the effect of the evolution of this oriented dislocation microstructure on the anisotropic hardening behavior. The model accounts for changes in the size, center, and shape, of the yield surface associated with isotropic, kinematic, and cross hardening, respectively. Identification of the model for the ferritic sheet metal steel LH800 is carried out with the help of shear, reverse shear, and tension–shear tests. The identified model has been validated using it to predict the stress–strain behavior of the material along different tension–shear loading paths and comparison with analogous experimental results. The results and in particular the comparison of theoretical predictions with experimental results clearly demonstrate the need of including cross hardening effects in the modeling of sheet metals like LH800.

1. Introduction

The experimental and theoretical characterization of sheet metal forming continues to present a number of challenges for theorist and experimentalist alike. Among the foremost issues in this regard is a realistic model for the material behavior. Metal forming processes generally involve large strain resulting in significant microstructural development and the development of different types of hardening. The influence of a developing microstructure on the hardening behavior in sheet metals has been the subject of many investigations (e.g., [1–15]). The nature and strength of this influence is strongly dependent on the type and complexity of the loading paths under consideration. As discussed for example by Barlat et al. [9], in the case of monotonic loading, the grain microstructure (i.e., texture) influences strongly the dependence of hardening on loading direction. In contrast, for loading paths with changes in direction, this behavior is dominated by the dislocation microstructure. Experimentally observed effects in this context include hardening stagnation after load reversal, and cross hardening after orthogonal loading. Experimental results exhibiting these effects exist for a number of different materials. Systematic studies of interstitial free (IF), high-strength low alloyed (HSLA), dual-phase (DP) and transformation-induced plasticity (TRIP), steels, as well as 5000 and 6000 series aluminum alloys, conducted by Bouvier et al. [11,13] found significant kinematic hardening, hardening stagnation, as well as cross hardening, especially for IF steels. In their investigations, the blank material was subjected to monotonic shear, reverse shear, as well as orthogonal tension–shear, loading. van Riel and van den Boogaard [16] have documented these effects in IF ferritic steels with the help of monotonic tension, reverse shear, and orthogonal tension–shear, tests, all under plane-strain conditions.

Perhaps the most well-known micromechanically based phenomenological model for anisotropic hardening on (non-proportional) loading paths characterized by directional changes is that of Teodosiu and Hu [1,2]. Besides accounting for isotropic and kinematic hardening, their model accounts for cross hardening via an evolving fourth-order tensor $\mathcal{S}$ influencing the effective yield stress in a loading-direction-dependent fashion. In the current back-rotated framework relevant to metals, the yield function for this model takes the form

$$\phi_{\mathrm{Teo}} = \sqrt{(\boldsymbol{M}-\boldsymbol{X})\cdot\mathcal{A}_{\mathrm{Teo}}\,(\boldsymbol{M}-\boldsymbol{X})} - \sigma_{\mathrm{Teo}}. \tag{1}$$

Here, $\boldsymbol{M}$ represents the Mandel stress, $\boldsymbol{X}$ the back stress, $\mathcal{A}_{\mathrm{Teo}}$ the Teodosiu flow anisotropy tensor, and σ_{Teo} the Teodosiu yield stress. In particular, $\mathcal{A}_{\mathrm{Teo}} \equiv \mathcal{A}_{\mathrm{Hill}}$ is modeled by the constant [17] initial flow anisotropy tensor $\mathcal{A}_{\mathrm{Hill}}$ determined by grain microstructure (i.e., texture). Further, $\sigma_{\mathrm{Teo}} \equiv \sigma_{\mathrm{Y0}} + r + f\,|\mathcal{S}|$ is determined by (i) the

* Corresponding author. Tel.: +49 231755 5717; fax: +49 231 755 2688.
E-mail address: muhammad.noman@tu-dortmund.de (M. Noman).

0921-5093/$ – see front matter © 2009 Elsevier B.V. All rights reserved.
doi:10.1016/j.msea.2009.12.013

initial yield stress σ_{Y0}, (ii) the increase r in this stress due to standard isotropic hardening, and (iii) the increase $f|\mathcal{S}|$ in this stress due to cross hardening. f represents the fraction of dislocation walls contributing to isotropic hardening whose strength in this sense is given by the magnitude $|\mathcal{S}| := \sqrt{\mathcal{S}\cdot\mathcal{S}} = \sqrt{S_{ijkl}S_{ijkl}}$ of $\mathcal{S}$. Since $\boldsymbol{M}$ and $\mathcal{S}$ are decoupled in ϕ_{Teo}, note that the evolution of $\mathcal{S}$ does not influence the form of the yield surface as represented by the dependence of ϕ_{Teo} on $\boldsymbol{M}$. For more details on this class of models as well as applications, the reader is referred to [15,18].

An alternative class of models for cross and more generally distortional hardening can be based on the approach of Baltov and Sawczuk [19]. In the current framework, this involves in particular a yield condition of the form

$$\phi_{\mathrm{Bal}} = \sqrt{(\boldsymbol{M}-\boldsymbol{X})\cdot\mathcal{A}_{\mathrm{Bal}}\,(\boldsymbol{M}-\boldsymbol{X})} - \sigma_{\mathrm{Bal}}, \tag{2}$$

with $\sigma_{\mathrm{Bal}} \equiv \sigma_{Y0} + r$. Besides the additional dependence of σ_{Teo} on $\mathcal{S}$, then, the basic difference between ϕ_{Teo} and ϕ_{Bal} lies in the fact that $\mathcal{A}_{\mathrm{Bal}}$ is not assumed constant. Its evolution is governed by a constitutive relation, and its initial value is given by $\mathcal{A}_{\mathrm{Hill}}$. A number of models for this evolution have been proposed in the literature, including the current one. For example, Voyiadjis and Foroozesh [20] proposed an evolution relation for $\mathcal{A}_{\mathrm{Bal}}$ based on three material parameters which mediate an assumed coupling between its principal directions and the effective stress $\boldsymbol{M}-\boldsymbol{X}$, resulting in asymmetric distortion of the yield surface. The model of Schick [21], which is based on the approach of Dafalias et al. [22], assumes multiple kinematic hardening mechanisms and a dependence of the evolution of $\mathcal{A}_{\mathrm{Bal}}$ on kinematic hardening in order to model yield surface development during tension–torsion loading [23]. Evolution of the yield surface has also been modeled by Yeganeh [24] in a rigid-plastic framework as based on the Hencky logarithmic strain. More recently, the model of Feigenbaum and Dafalias [25] involves an evolution relation for $\mathcal{A}_{\mathrm{Bal}}$ coupled to the magnitude of the effective stress and the projection of the direction of the effective stress onto the back stress. This leads to an asymmetric distortion of the yield surface with increasing curvature in the direction of distortion in stress space. In Feigenbaum and Dafalias [26], a simplified version of such a model is developed in which there is no coupling to the evolution of the back stress. Development of these types of models has been motivated by tension–torsion experiments on aluminum and steel tubes (e.g., Phillips et al. [27], Boucher and Cordebois [28], Ishikawa [23]). In Phillips et al. [27], Boucher and Cordebois [28], a distortion of the yield surface in the direction of applied stress was determined. This involved an increase in curvature of the yield surface in this direction and a corresponding decrease in curvature in the opposite direction.

The purpose of the current work is to introduce and validate a new model for cross hardening and hardening stagnation during orthogonal loading in the context of the approach of [19]. This is based on an evolution relation for $\mathcal{A}_{\mathrm{Bal}}$ accounting for the effects of an evolving dislocation microstructure on the hardening behavior. Like many of the models discussed above, the initial value of $\mathcal{A}_{\mathrm{Bal}}$ is determined in the current model by the grain microstructure (i.e., texture). In contrast to these models, however, the current form of the evolution relation for $\mathcal{A}_{\mathrm{Bal}}$ is directly motivated by the evolution of the cell-wall dislocation microstructure (e.g., Nesterova et al. [29]) during loading-path changes and its effect on hardening. An analogous form was formulated for $\mathcal{S}$ in the model of Wang et al. [15]. On the one hand, this results in a model which is simpler than either that of Teodosiu and Hu [2] or Wang et al. [15] and contains fewer material parameters. On the other hand, the current model is not capable of representing hardening stagnation after reverse loading. Micromechanical support for working with a model based on (2) rather than on (1), i.e., with a model in which cross hardening is associated with a change in the shape of the yield surface, i.e., distortional hardening, comes for example from the very interesting work of Peeters et al. [8]. They worked with a polycrystal model based on fully constraint Taylor-based homogenization which takes the evolution of the dislocation microstructure into account at the grain level in an effective fashion. Using this approach, they were able to simulate the cross effect in orthogonal tension–shear tests and a corresponding change in shape of the yield surface. In particular, the development of dislocation walls at the grain level during proportional loading corresponds to the expansion of the yield surface into directions orthogonal to the loading direction. On the other hand, the development of localization bands and the breakdown of existing dislocation structures after orthogonal change of direction leads to yield surface shrinkage in the new direction of loading. Besides the stress–strain- and loading-path-based data which will be presented in this work, that of Ishikawa [23] for yield surface development in the stainless steel SUS304 during tension–torsion exhibits (some of) these effects and in particular a change in shape of the yield surface.

The current work begins in Section 2 with a formulation of the current model in the framework of the multiplicative decomposition of the deformation gradient and the assumption of small elastic strain relevant to metal inelasticity. In order to identify and validate the model, tension–shear and cyclic shear tests on the ferritic steel LH800 Tekkaya et al. [30] have been carried out. The experimental setup and details of these tests together with the basic data are presented in Section 3. The strategy developed for the model identification together with the results of this identification are discussed in Section 4. The model is also validated in this section with the help of additional test results for other strain paths not used in the model identification. Lastly, in Section 5, the identified model is used to investigate the evolution of the yield surface and that of inelastic state with respect to loading-path history. Finally, the work ends in Section 6 with a discussion and conclusions.

2. Model formulation

The phenomenological representation of evolving hardening behavior in terms of changes in the size, center and shape of the yield surface offers the means to characterize the behavior of the steels of interest during complex, non-proportional loading processes present in many technological processes (e.g., deep-drawing). The challenge lies in the connection of such changes in the yield surface geometry with the underlying microscopic and physical mechanisms of grain and dislocation microstructural development in polycrystalline metals. One basic expectation in this regard is that the grain microstructure in sheet metals is determined almost solely by the rolling process. Forming processes like cup drawing are expected to result in little or no change in this microstructure. Consequently, during forming processes, yield surface evolution is generally expected to be due almost solely to an evolving dislocation microstructure at the grain- or grain-cluster level. This is the focus of the current model.

The formulation of the current model is carried out in the framework of the standard inelastic multiplicative decomposition $\boldsymbol{F} = \boldsymbol{F}_{\mathrm{E}}\boldsymbol{F}_{\mathrm{P}}$ of the deformation gradient $\boldsymbol{F}$ (e.g., Simo and Hughes [31]). Such a decomposition arises naturally, e.g., in the context of the modeling of $\boldsymbol{F}_{\mathrm{P}}$ as a change of local reference configuration [32]. In this context, one obtains in particular the result

$$\boldsymbol{R}_{\mathrm{E}}^{\mathrm{T}}\boldsymbol{L}_{\mathrm{E}}\boldsymbol{R}_{\mathrm{E}} = \boldsymbol{R}_{\mathrm{E}}^{\mathrm{T}}\boldsymbol{L}\boldsymbol{R}_{\mathrm{E}} - \boldsymbol{U}_{\mathrm{E}}\boldsymbol{L}_{\mathrm{P}}\boldsymbol{U}_{\mathrm{E}}^{-1} = \boldsymbol{R}_{\mathrm{E}}^{\mathrm{T}}\dot{\boldsymbol{R}}_{\mathrm{E}} + \dot{\boldsymbol{U}}_{\mathrm{E}}\boldsymbol{U}_{\mathrm{E}}^{-1} \tag{3}$$

via the right polar decomposition $\boldsymbol{F}_{\mathrm{E}} = \boldsymbol{R}_{\mathrm{E}}\boldsymbol{U}_{\mathrm{E}}$ of $\boldsymbol{F}_{\mathrm{E}}$ for the back-rotated form of $\boldsymbol{L}_{\mathrm{E}} := \dot{\boldsymbol{F}}_{\mathrm{E}}\boldsymbol{F}_{\mathrm{E}}^{-1}$ in terms of $\boldsymbol{L} := \dot{\boldsymbol{F}}\boldsymbol{F}^{-1}$ and $\boldsymbol{L}_{\mathrm{P}} := \dot{\boldsymbol{F}}_{\mathrm{P}}\boldsymbol{F}_{\mathrm{P}}^{-1}$. For the current case of polycrystalline metals and small elastic

strain, we have

$$\begin{aligned} &\boldsymbol{U}_{\mathrm{E}} \approx \boldsymbol{I} + \ln \boldsymbol{U}_{\mathrm{E}}, \\ &\dot{\boldsymbol{U}}_{\mathrm{E}} \boldsymbol{U}_{\mathrm{E}}^{-1} \approx \overline{\ln \boldsymbol{U}}_{\mathrm{E}}. \end{aligned} \tag{4}$$

Substituting these into (3), and taking the symmetric and skew-symmetric parts of the result, one obtains the evolution relations

$$\begin{aligned} &\overline{\ln \boldsymbol{U}}_{\mathrm{E}} = \boldsymbol{R}_{\mathrm{E}}^{\mathrm{T}} \boldsymbol{D} \boldsymbol{R}_{\mathrm{E}} - \boldsymbol{D}_{\mathrm{P}}, \\ &\dot{\boldsymbol{R}}_{\mathrm{E}} = \boldsymbol{W} \boldsymbol{R}_{\mathrm{E}} - \boldsymbol{R}_{\mathrm{E}} \boldsymbol{W}_{\mathrm{P}}, \end{aligned} \tag{5}$$

for $\ln \boldsymbol{U}_{\mathrm{E}}$ and $\boldsymbol{R}_{\mathrm{E}}$, respectively, in the incremental context. $\boldsymbol{D} := \mathrm{sym}(\boldsymbol{L})$ is the continuum rate of deformation, $\boldsymbol{D}_{\mathrm{P}} := \mathrm{sym}(\boldsymbol{L}_{\mathrm{P}})$ its inelastic counterpart, $\boldsymbol{W} := \mathrm{skw}(\boldsymbol{L})$ the continuum spin, and $\boldsymbol{W}_{\mathrm{P}} := \mathrm{skw}(\boldsymbol{L}_{\mathrm{P}})$ the plastic spin. Restricting the current formulation to the case of sheet metal forming, it is reasonable to assume that the texture in these materials achieved during rolling remains largely unchanged during forming processes like tension, compression, simple shear, cyclic simple shear, and combinations of these. In this case, $\boldsymbol{W}_{\mathrm{P}}$ is negligible, and the evolution of $\boldsymbol{R}_{\mathrm{E}}$ depends only on $\boldsymbol{W}$, in which case it reduces to a purely kinematic quantity (i.e., the Jaumann rotation). In addition, focusing in this work on the material behavior of sheet metal during forming below the forming limit, we assume for simplicity that damage or any other process resulting in inelastic volume changes are negligible. In this case, plastic incompressibility $\det(\boldsymbol{F}_{\mathrm{P}}) = 1$ pertains, implying $\mathrm{tr}(\boldsymbol{D}_{\mathrm{P}}) = 0$ and $\boldsymbol{D}'_{\mathrm{P}} = \boldsymbol{D}_{\mathrm{P}}$ in the incremental context.

Since the elastic range and elastic strain are small, any texture effects from rolling leading to an anisotropic elastic behavior are assumed negligible. In this case, the isotropic form

$$\boldsymbol{M} = \kappa\, \mathrm{tr}(\boldsymbol{E}_{\mathrm{E}})\, \boldsymbol{I} + 2\mu \boldsymbol{E}'_{\mathrm{E}} \tag{6}$$

is assumed for the Mandel stress $\boldsymbol{M}$ in terms of the elastic strain $\boldsymbol{E}_{\mathrm{E}} := \ln \boldsymbol{U}_{\mathrm{E}}$, bulk modulus κ, shear modulus μ, and deviatoric part $\boldsymbol{E}'_{\mathrm{E}}$ of $\boldsymbol{E}_{\mathrm{E}}$. Lastly, again in the framework of small elastic strain, $\boldsymbol{M}$ and $\boldsymbol{R}_{\mathrm{E}}$ determine the Kirchhoff stress $\boldsymbol{K}$ via

$$\boldsymbol{K} = \boldsymbol{R}_{\mathrm{E}} \boldsymbol{M} \boldsymbol{R}_{\mathrm{E}}^{\mathrm{T}}. \tag{7}$$

Consequently, in contrast to $\boldsymbol{K}' = \boldsymbol{R}_{\mathrm{E}} \boldsymbol{M}' \boldsymbol{R}_{\mathrm{E}}^{\mathrm{T}}$, $\mathrm{tr}(\boldsymbol{K}) = \mathrm{tr}(\boldsymbol{M})$ of $\boldsymbol{K}$ is independent of $\boldsymbol{R}_{\mathrm{E}}$.

In this framework, then, the material behavior of polycrystalline sheet metal during forming processes below the forming limit is predominantly determined by a changing dislocation microstructure and attendant evolving anisotropic yield behavior. Besides a shift of the yield surface and its proportional expansion as in the case of conventional combined hardening, the current model also accounts for an evolving yield surface shape and so distortional hardening. As discussed in the introduction, this model is based in particular on a yield function of the form (2) from Baltov and Sawczuk [19]. In the current notation, this is written simply in the form

$$\phi = \sqrt{(\boldsymbol{M} - \boldsymbol{X}) \cdot \mathcal{A} (\boldsymbol{M} - \boldsymbol{X})} - \sigma_{\mathrm{Y0}} - r \tag{8}$$

in terms of the initial yield stress σ_{Y0}. For the class of materials under consideration, the saturation (i.e., Voce) form

$$\dot{r} = c_r (s_r - r)\, \dot{\alpha}_{\mathrm{P}} \tag{9}$$

for the evolution of r is appropriate, driven by that of the equivalent inelastic deformation α_{P}. Here, c_r represents the rate, and s_r the value, for saturation associated with r. Since σ_{Y0} is the initial yield stress (i.e., for $\alpha_{\mathrm{P}} = 0$), the initial value r_0 of r is zero. In the current rate-independent context, α_{P} is determined as usual by the consistency condition. Analogous to isotropic hardening, kinematic hardening is modeled via the saturation (i.e., Armstrong–Frederick) form

$$\dot{\boldsymbol{X}} = c_x (s_x \boldsymbol{N}_{\mathrm{P}} - \boldsymbol{X})\, \dot{\alpha}_{\mathrm{P}} \tag{10}$$

for the evolution of $\boldsymbol{X}$ depending on corresponding (constant) saturation rate c_x, (constant) saturation magnitude s_x, as well as the (variable) direction $\boldsymbol{N}_{\mathrm{P}} := \boldsymbol{D}_{\mathrm{P}}/|\boldsymbol{D}_{\mathrm{P}}|$ of the rate of inelastic deformation

$$\boldsymbol{D}_{\mathrm{P}} = \dot{\alpha}_{\mathrm{P}} \partial_{\boldsymbol{M}-\boldsymbol{X}} \phi, \tag{11}$$

which is modeled here in associated form. The initial value of $\boldsymbol{X}$ is assumed to be zero.

The constitutive model formulation is completed by an evolution relation for $\mathcal{A}$ in order to represent the effect of cross hardening on the material behavior. The form of this relation introduced in what follows is based on the idea that active or "dynamic" dislocation microstructures oriented with respect to the current loading direction (idealized in the model context by $\boldsymbol{N}_{\mathrm{P}}$) persist and become inactive or "latent" after a loading-path change and strengthen existing obstacles to glide-system activation in the new loading direction. In addition, both dynamic and latent dislocation structures are assumed to saturate with increasing accumulated inelastic deformation. These assumptions are built into the constitutive relation

$$\dot{\mathcal{A}} = c_d (s_d \boldsymbol{N}_{\mathrm{P}} \otimes \boldsymbol{N}_{\mathrm{P}} - \mathcal{A}_d)\, \dot{\alpha}_{\mathrm{P}} + c_l \{ s_l (\mathcal{I}_{\mathrm{dev}} - \boldsymbol{N}_{\mathrm{P}} \otimes \boldsymbol{N}_{\mathrm{P}}) - \mathcal{A}_l \}\, \dot{\alpha}_{\mathrm{P}} \tag{12}$$

for the evolution of $\mathcal{A}$. Here, $\mathcal{I}_{\mathrm{dev}}$ is the deviatoric part of the fourth-order identity tensor, and

$$\begin{aligned} &\mathcal{A}_d := (\boldsymbol{N}_{\mathrm{P}} \cdot \mathcal{A} \boldsymbol{N}_{\mathrm{P}})\, \boldsymbol{N}_{\mathrm{P}} \otimes \boldsymbol{N}_{\mathrm{P}}, \\ &\mathcal{A}_l := \mathcal{A} - \mathcal{A}_d, \end{aligned} \tag{13}$$

represent the "dynamic" and "latent" parts of $\mathcal{A}$, respectively. More precisely, these are the projections of $\mathcal{A}$ parallel and orthogonal, respectively, to the current (instantaneous) inelastic flow direction $\boldsymbol{N}_{\mathrm{P}}$. The first term in (12) is of the saturation type with respect to $\mathcal{A}_d$, with c_d the rate of saturation, and $s_d \boldsymbol{N}_{\mathrm{P}} \otimes \boldsymbol{N}_{\mathrm{P}}$ the saturation value, respectively, of $\mathcal{A}_d$. Likewise, c_l is the saturation rate, and $s_l (\mathcal{I}_{\mathrm{dev}} - \boldsymbol{N}_{\mathrm{P}} \otimes \boldsymbol{N}_{\mathrm{P}})$ the saturation value, of $\mathcal{A}_l$. The initial value $\mathcal{A}_0$ of $\mathcal{A}$ is determined by any Hill initial flow orthotropy due to any texture from rolling. In contrast to some of the models discussed in the introduction, e.g., Teodosiu and Hu [2], Wang et al. [15] or Dafalias et al. [22], Feigenbaum and Dafalias [25] note that there is no direct coupling between kinematic and distortional hardening in the current model. This is also the case in the recent model of Feigenbaum and Dafalias [26], which focuses on the asymmetric development of the yield surface rather than on the effect of cross hardening as is done in the current work.

The current material model was implemented in the commercial FE codes Abaqus and LS-Dyna via the user material interfaces provided. Besides the two elasticity parameters κ, μ and the 6 parameters (e.g., in the sense of Hill: F, G, H, L, M, N) for the initial flow orthotropy, this model contains 8 hardening parameters $c_r, s_r, c_x, s_x, c_d, s_d, c_l, s_l$ to be identified using the tests to be described next.

3. Material testing

The experimental work has been carried out on a biaxial testing device capable of loading a sheet metal specimen in both simple shear and in plane-strain tension. Using this device, one can carry out single- or multi-stage loading programs consisting of monotonic (e.g., forward simple-shear), reverse (e.g., forward-reverse simple-shear), and/or orthogonal (e.g., tension–shear), changes of loading direction. In particular, the latter can be carried out with or without unloading of the specimen upon change of loading direction.

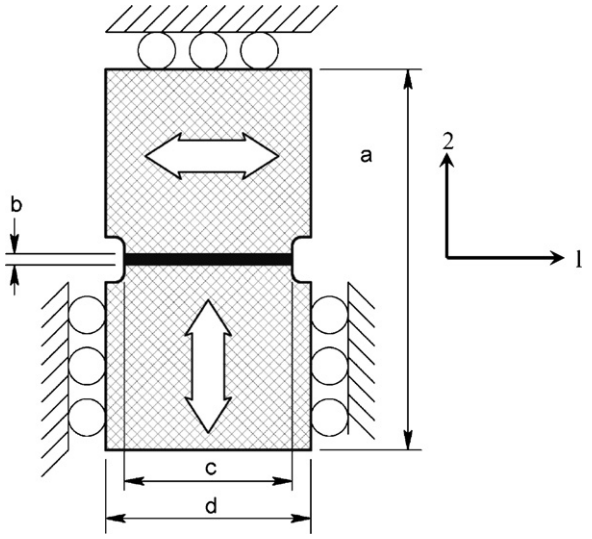

Fig. 1. Biaxial test setup. Geometry of the tension–shear specimen and the measurement region of height b and width c. The checkered region indicates the actual specimen and the black area marks the actual deformation zone. The tension direction is direction 2 and the shear direction is direction 1.

3.1. Test setup

The biaxial testing equipment had been developed at the University of Twente. It consists of a regular uniaxial testing device which via an actuator is used to achieve plane-strain tension in the sample. A subframe mounted between the cross bars accommodates the actuator for simple shear deformation. The deformation is applied to the sample as indicated in Fig. 1.

The ratio of the height (b) of the measurement region to the sample thickness is chosen in order to minimize the chance of buckling during simple shear. In addition, to achieve homogeneous deformation in the measurement area c/b is large as shown in Fig. 1. The deformation is measured in an area within the deformation zone. The notched boundary then constrains the specimen in the transverse direction during tension or shear, resulting in plane-strain conditions.

The deformation field is determined by optical measurement (in a procedure comparable to the commercially available ARAMIS system). To this end, the motion of an array of sixteen black silicon dots painted on the surface of the measurement area are tracked and recorded with a camera. The relative motion of these dots is used to calculate the deformation gradient via a least-squares method. During a test, two sensors on the actuators record the force achieved in shear and in tension. Using the known geometry of the specimen, these force measurements are used to calculate the Cauchy tensile and shear stress, T_{22} and T_{12}, respectively. The plane-strain tension and simple shear tests represent the boundaries of the range of stress states achievable in the specimen with the help of the biaxial testing device (Fig. 1). By applying different combinations of simple shear and plane-strain tension, different stress states on the yield surface are achieved. The exact position of the yield state in principal stress space, however, is unknown since the transverse stress cannot be measured. Further details of the experimental setup can be found in van Riel and van den Boogaard [16].

3.2. Test results

For the current work, tests performed on specimens of the ferritic steel LH800 include (i) monotonic plane-strain tension at different strain-rates, (ii) reverse simple-shear for different amounts of forward pre-shear, and (iii) orthogonal tension–shear

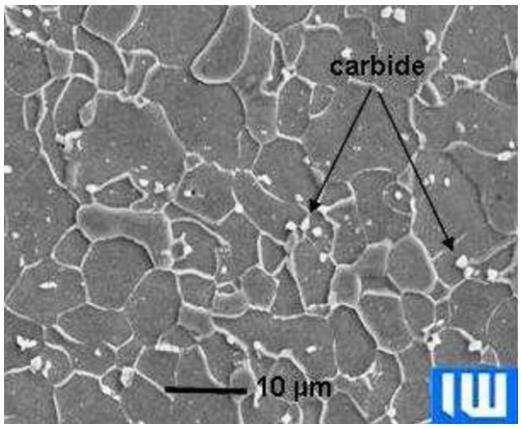

Fig. 2. Scanning electron micrograph showing microstructure of LH800 (Experiment IW Hannover).

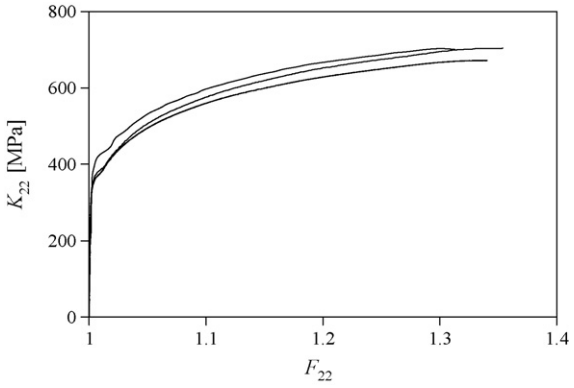

Fig. 3. Tension test results for LH800 at strain rates of 10^{-1} s^{-1} (upper curve), 10^{-2} s^{-1} (middle curve), 10^{-3} s^{-1} (lowest curve). K_{22} represents the relevant component of the Kirchhoff stress and F_{22} represents the relevant component of the deformation gradient.

with and without unloading. This sheet steel is characterized by an initial texture consisting of fine-grained ferrite, grain size of approximately 8 μm in diameter, see Fig. 2 Tekkaya et al. [30]. The thickness of the sheet metal specimens used in all the tests was 0.7 mm. All tests were preformed with the tension direction oriented in the rolling direction.

Consider first the monotonic plane-strain tension tests. As stated above, these have been performed at different strain rates. Fig. 3 displays the corresponding results.

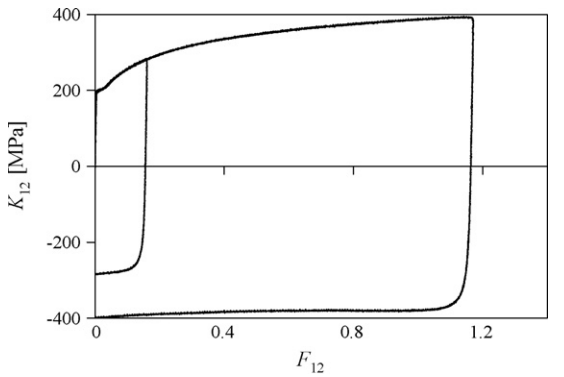

Fig. 4. Reverse shear test results for LH800 for two different levels (i.e., 0.1 and 0.65) of pre-shear. All stress results are shown in absolute value form.

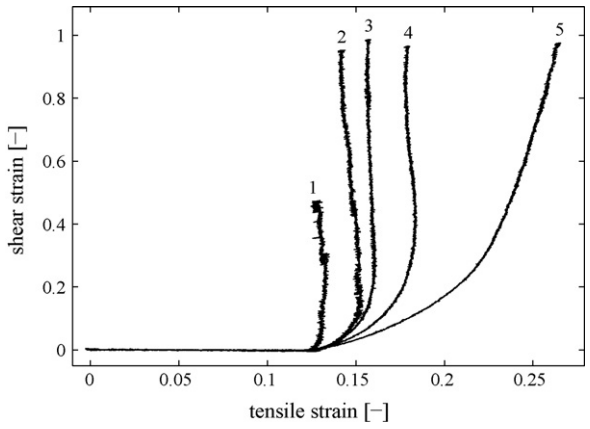

Fig. 5. Experimental strain paths in LH800 resulting from continuous change of loading direction from tension to shear.

As observed in many metals, the flow stress in LH800 increases as a function of increasing strain-rate. The remaining tests have been performed under quasi-static conditions (i.e., 10^{-3} s^{-1}). Fig. 4 shows the results of 2 reverse simple-shear tests. The elastic–inelastic transition for this material upon load reversal is very diffuse. The Bauschinger effect is clearly present. It would appear that the amount of pre-shear does not influence the magnitude of the Bauschinger effect significantly. On the other hand, the test with the larger pre-shear is clearly closer to the hardening saturation level. Hardening stagnation after load reversal is clearly visible in both cases, but less pronounced at lower pre-shear.

Lastly, consider the results from the orthogonal tests. As stated above, these consist of plane-strain tension followed by simple shear loading. The transition from tension to simple shear is either discontinuous via intermediate unloading, or continuous without unloading. The data so obtained include the 5 different continuous loading paths (numbered 1 to 5) shown in Figs. 5 and 6.

Consistent with existing interpretations of such data in the literature, the presence or absence of cross hardening in such orthogonal tests is judged solely by comparison with the monotonic simple shear results. In particular, any overshoot of the yield stress above the monotonic level upon transition from tension to shear is an indicator of such hardening. Using this "definition," curves 1, 2 and 3 in Fig. 5 clearly exhibit cross hardening as can be seen in Fig. 6, curve 4 might exhibit a little, and curve 5 clearly none at all. In the one extreme (path 1), the orthogonal change is realized via an "abrupt" reduction in tension and coincident increase in shear at yield. This is closest to the case of a discontinuous orthogonal loading-path change as shown in Fig. 7.

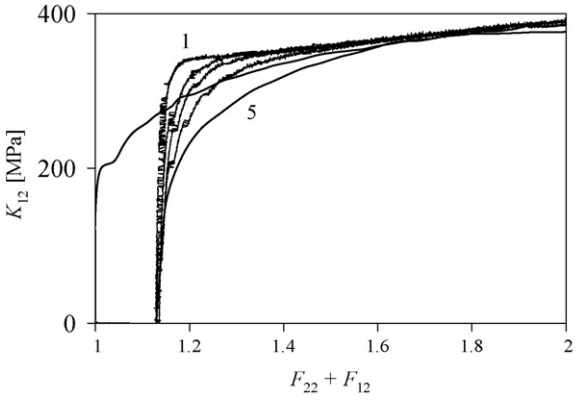

Fig. 6. Stress response of LH800 for monotonic forward simple shear (curve starting at $F_{22} = 1$) and for the 5 different orthogonal tension–shear paths shown in Fig. 5.

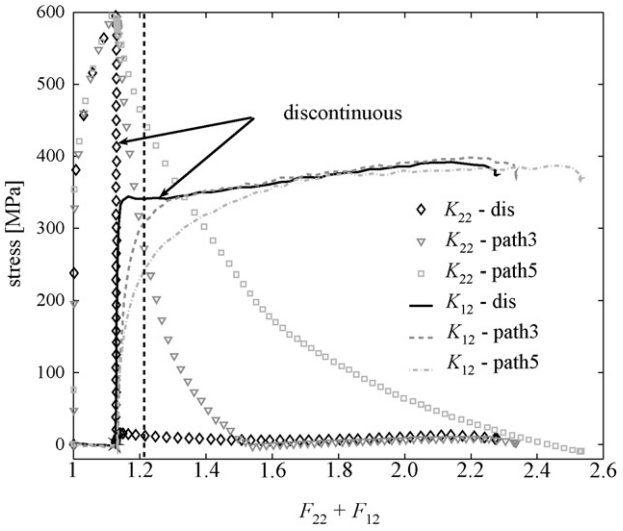

Fig. 7. Discontinuous and continuous orthogonal loading-path changes from tension to shear in LH800. Normal stress component K_{22} (symbols) and shear stress component K_{12} (lines) as a function of $F_{22} + F_{12}$. The vertical dashed line indicates deformation states of equal $F_{22} + F_{12}$.

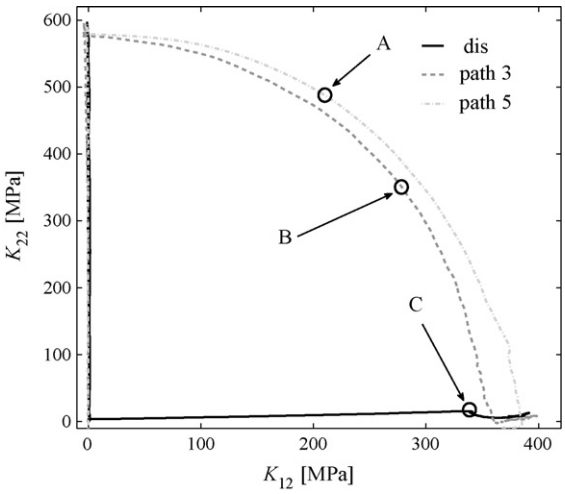

Fig. 8. Experimental paths in (K_{22}, K_{12}) stress space corresponding to selected paths shown in Figs. 5 and 7. Points A, B and C mark the state of deformation corresponding to the intersection of the vertical dashed line in Fig. 7 with the respective stress curves.

In the other extreme (path 5), the level of tension is maintained (and further tensile deformation occurs) as shear loading increases. As indicated, the other three paths (2, 3, and 4) in Fig. 5 represent intermediate cases between these extremes.

In Fig. 8, the paths in the (K_{12}, K_{22}) stress plane are shown which correspond to (i) discontinuous orthogonal loading (curve "dis" in Fig. 7) as well as, from Fig. 5, (ii) continuous orthogonal loading path 3, and (iii) continuous orthogonal loading path 5.

The stress states A, B and C correspond to deformation states of equal $F_{22} + F_{12}$ which intersect continuous path 5, continuous path 3, and the discontinuous path, respectively. The intersections of the vertical dashed line in Fig. 7 with the stress curves mark the same points, but in stress-deformation space. As implied by these results, the nature of the transition from tension to shear is crucial in determining whether or not cross hardening occurs, e.g., the increase in the yield stress above the monotonic shear level after an orthogonal change in loading path from tension to shear. Beyond being associated with stress states on the yield surface

Table 1
Identified hardening model parameter values for LH800.

	Value	Units
(a) Isotropic hardening parameter values determined from monotonic simple-shear test data alone		
s_r	341.50	MPa
c_r	5.82	
(b) Isotropic–kinematic hardening parameters determined from monotonic and cyclic simple-shear test data alone		
s_r	245.684	MPa
c_r	4.295	
s_x	97.464	MPa
c_x	33.642	

which are not influenced by cross hardening, cases 4 and 5 exhibit basically no cross hardening and are characterized by the fact that significant further tension loading takes place after the start of the shear loading phase. Assuming that the dislocation microstructure developed during the common pre-tension phase was the same in each case, these results imply that continued tension loading during simultaneous shear loading at yield facilitates a breakdown of tension-based dislocation microstructure which would otherwise result in cross hardening upon transition to shear. Besides this, note that the paths with continued tension loading do not return to the monotonic simple-shear reference curve, i.e., at least not within the range of the experimental data. These and other aspects will be examined in more detail after we carry out the model identification, to which we now turn.

4. Model identification

To demonstrate the capability of the presented model to describe the complex hardening behavior of LH800 during non-proportional loading just discussed, we now turn to its identification. As shown by the experimental data in the last section, this behavior involves in particular isotropic, kinematic, and cross hardening. The material parameter determination is carried out using the program LS-OPT in conjunction with LS-DYNA. Given the homogeneous nature of the tests, one-element calculations suffice. The optimization technique used relies on response surface methodology (RSM) Stander et al. [33]. Other methods have been used by previous workers (e.g., Haddadi et al. [34], Flores et al. [35]) to identify related models like the Teodosiu model.

All fits to follow are based on the fixed values $\kappa = 167.05$ GPa and $\mu = 77.09$ GPa for the elastic properties, as well as that $\sigma_{Y0} = 330.79$ MPa for the initial yield stress, of LH800, all at room temperature. Tensile tests performed on LH800 at 0°, 45°, 90° with respect to the rolling direction yielded no distinct initial orthotropy and so Hill parameter values of $F = G = H = 0.5$ and $L = M = N = 1.5$. Strictly speaking, only N, F, G and H can be determined by in-plane tensile tests. Isotropy is also in essence tacitly assumed for the case of through-thickness shear. The fit procedure for the hardening model begins by using monotonic simple-shear test data to identify the Voce isotropic hardening model alone, i.e., assuming no kinematic or cross hardening. The results of this fit are shown in Table 1(a). The quality of the fit can be judged via the comparison of the fitted model with the data in Fig. 9.

The isotropic hardening parameters so determined are then used as starting values to identify the isotropic–kinematic hardening model parameters using both monotonic and cyclic simple-shear test data. The results of this are shown in Table 1(b). The quality of the model identification can be judged via comparison with the fit data as shown for the current combined (isotropic–kinematic) case in Fig. 10.

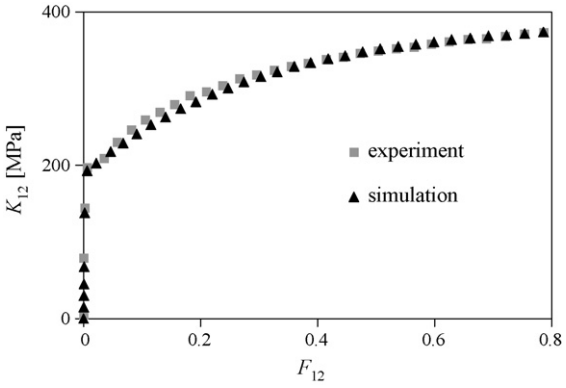

Fig. 9. Comparison of the experimental monotonic simple-shear data with the corresponding identified model prediction. K_{12} represents the relevant shear component of the Kirchhoff stress.

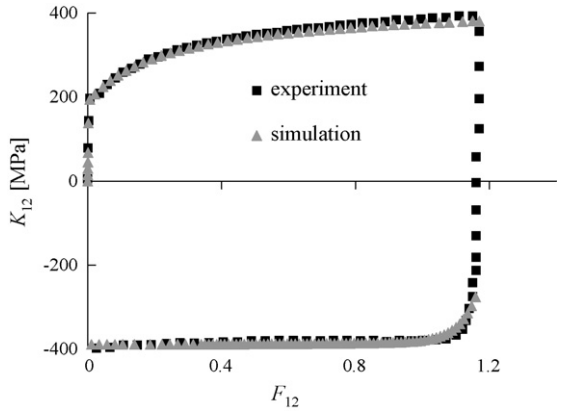

Fig. 10. Comparison of the experimental cyclic simple-shear data with the corresponding identified combined isotropic–kinematic model prediction.

As can be seen in Fig. 9, we use the experimentally determined components of the deformation gradient $\boldsymbol{F}$ to parameterize the experimental data for the model identification procedure. This is in contrast to the standard practice of using the accumulated equivalent inelastic deformation α_P for this purpose, which is a model quantity and therefore not experimentally determined. Note that these parameterizations are not equivalent. This can also be seen from the fact that one obtains different model parameter values than those in Table 1 when using α_P in this way. For example, in the combined isotropic–kinematic hardening case, one obtains

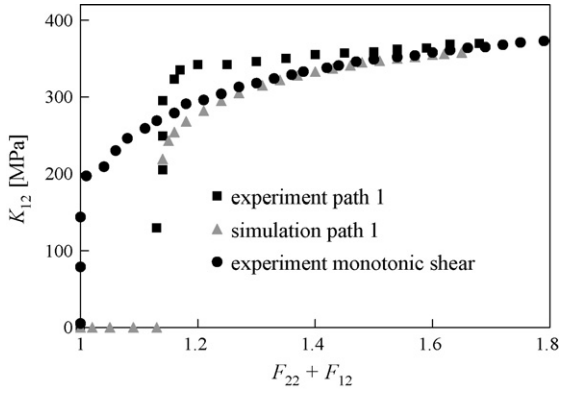

Fig. 11. Comparison of the predictions of the identified standard combined (i.e., isotropic–kinematic) hardening model for forward simple shear and orthogonal tension–shear with corresponding experimental results from path 1 in Fig. 5.

Table 2
Identified hardening model parameter values for LH800 for isotropic–kinematic–cross hardening model parameter values determined from monotonic shear, cyclic shear, and orthogonal tension–shear, test data.

	Value	Units
s_r	254.519	MPa
c_r	4.481	
s_x	90.896	MPa
c_x	32.695	
s_d	0.0	
c_d	19.712	
s_l	−0.863	
c_l	5.0	

$c_r = 2.96, s_r = 219.37, c_x = 15.19, s_x = 139.63$ instead of the values shown in Table 1(b), as well as a poorer fit.

Before we proceed to the identification of the complete hardening model, it is instructive to compare the predictions of the identified standard combined (i.e., isotropic–kinematic) hardening model for orthogonal tension–shear loading with the corresponding test data as represented by path 1 in Fig. 5. This is done in Fig. 11.

Not surprisingly, the model predicts no cross hardening. Optically, one might be tempted to identify the prediction of the identified combined isotropic–kinematic model with case 4 or 5 in Fig. 5. Since these represent different paths in either strain or stress space, however, they are not directly comparable.

Consider lastly the identification of the isotropic–kinematic–cross (i.e., complete) hardening model. Again, this is done with the help of the identified parameter values for the isotropic–kinematic case as starting values. In this way, the complete model is fit to monotonic shear, cyclic shear, and orthogonal tension–shear, test data. In particular, the test data of path 1 in Fig. 5 is added to the previous monotonic shear and cyclic shear data sets. As with c_r and c_x, the saturation rates c_d and c_l associated with cross hardening are constrained to be greater than zero in the fit. On the other hand, as with s_r and s_x, s_d and s_l may be positive or negative. Since the values for s_d determined in this way were on the order of 10^{-3}, this parameter was set to zero in the final fits, resulting in the parameter values for the complete model shown in Table 2. A comparison of the corresponding experimental data and model fit is shown in Fig. 12.

As a first validation of the identified hardening model, this is used to simulate the behavior of LH800 along the experimental strain paths 2 to 5 in Fig. 5 not used in the identification procedure. The results of this are shown in Figs. 13 and 14.

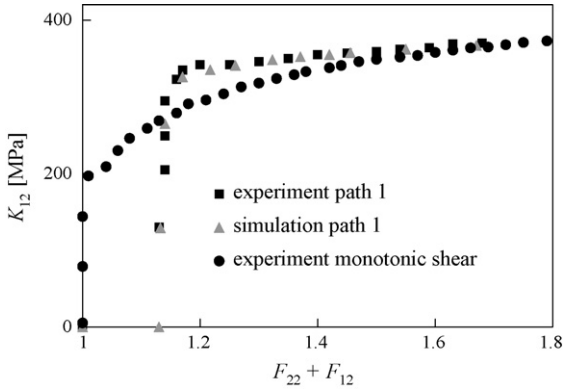

Fig. 12. Comparison of identified isotropic–kinematic–cross hardening model behavior with experimental data for monotonic simple-shear and orthogonal tension–shear test data corresponding to strain path 1 in Fig. 5.

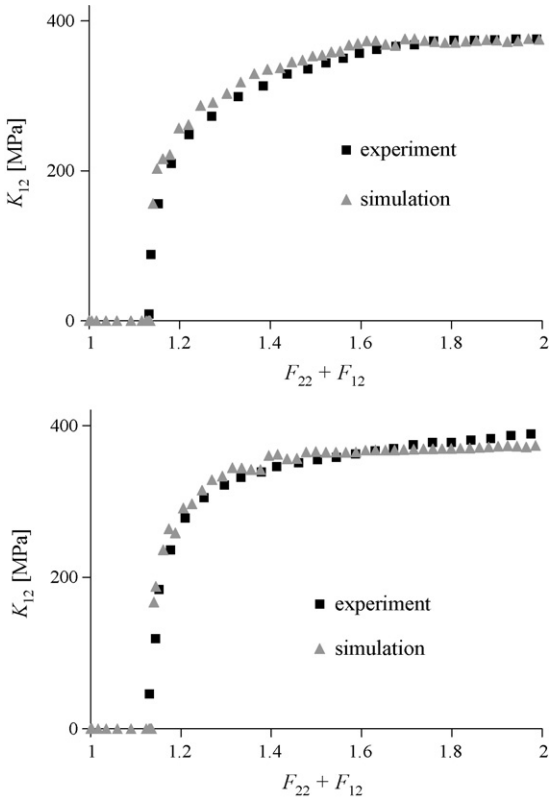

Fig. 13. Comparison of the experimental results for strain paths 5 and 4 in Fig. 5 with corresponding simulation results as based on the identified model for isotropic–kinematic–cross hardening. Top: path 5. Bottom: path 4.

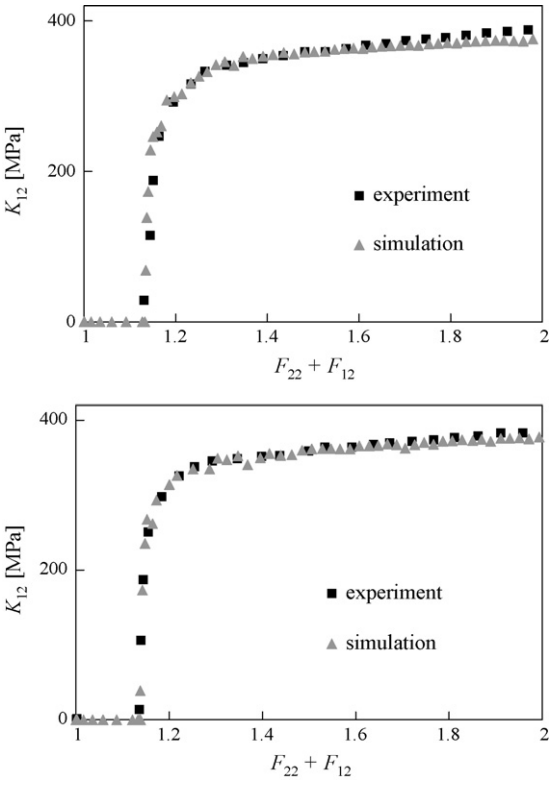

Fig. 14. Comparison of the experimental results for strain paths 3 and 2 in Fig. 5 with corresponding simulation results as based on the identified model for isotropic–kinematic–cross hardening. Top: path 3. Bottom: path 2.

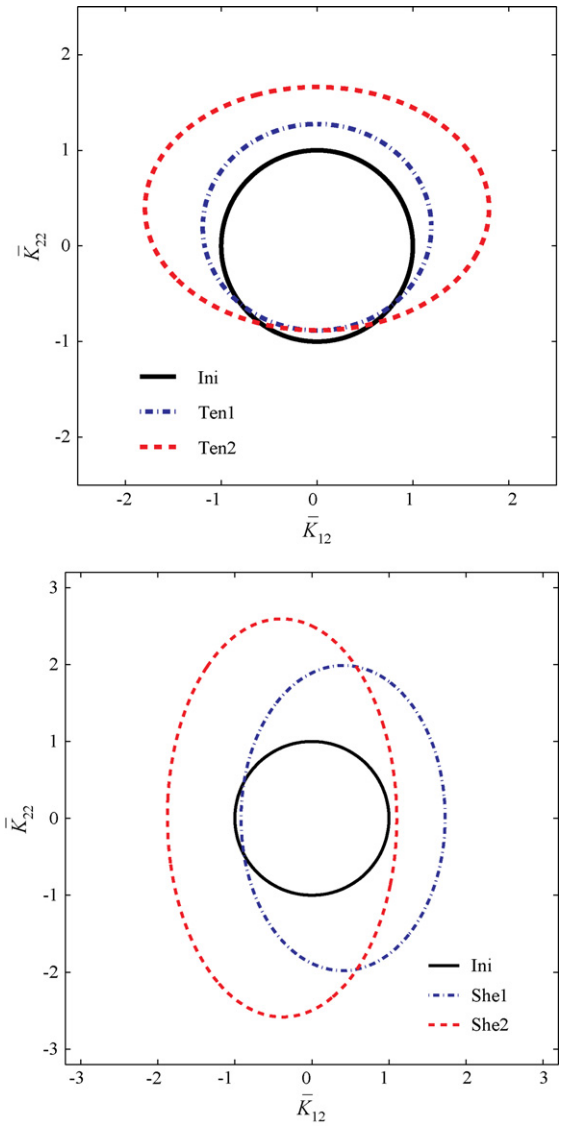

Fig. 15. Yield surface evolution for LH800 during uniaxial tension (top) and simple shear (bottom). Shown here are the initial surface (Ini), an intermediate tension state (Ten1), the final tension state at $F_{22} = 1.2$ (Ten2), the final forward shear state at $F_{12} = 0.4$ (She1), and the final reverse shear state at $F_{12} = 0.0$ (She2).

Clearly, the agreement between experimental and simulation results is good. Beyond a realistic representation of complete isotropic–kinematic–cross hardening behavior, then, the current model is also capable of accounting for the dependence of cross hardening on the nature and details of the orthogonal transition from tension to shear. To investigate this further, we turn next to examine the implications of the model for yield surface and internal state development during monotonic shear, cyclic shear and orthogonal tension–shear loading processes.

5. Yield surface evolution

Having established the ability of the current model to represent the development of combined isotropic–kinematic–cross hardening in LH800 during non-proportional loading, we now turn to a discussion of the evolution of the yield surface. To begin, consider the yield surface evolution for LH800 predicted by the identified model from the previous section. To this end, we look at the cases of (i) uniaxial tension, (ii) simple shear, (iii) plane-strain tension followed by simple shear and, (iv) a continuous transition from

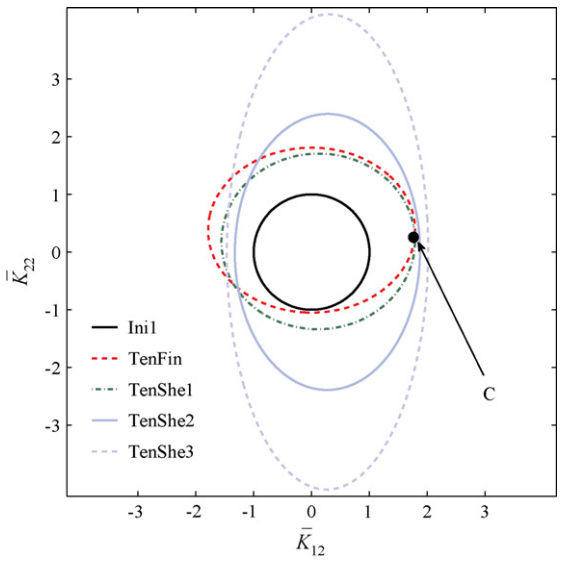

Fig. 16. Predicted yield surface evolution for LH800 during orthogonal loading from plane-strain tension to simple-shear depicted in normalized stress space $(\bar{K}_{12}, \bar{K}_{22})$ for the discontinuous transition. Ini represents the initial yield surface. TenFin is the final tensile state. TenShe1 to TenShe3 represent subsequent yield surfaces during subsequent loading for the loading path also shown in Figs. 5 and 7. The point C indicates the stress state obtained during the experiment and is the same point C as shown in Fig. 8.

plane-strain tension to simple shear. For representation purposes, we work with the normalized shear $\bar{K}_{12} := \sqrt{3}K_{12}/\sigma_{Y0}$ and normal $\bar{K}_{22} := K_{22}/\sigma_{Y0}$ stress components. For example, an isotropic yield surface in $(\bar{K}_{12}, \bar{K}_{22})$-space takes the form of the unit circle. The resulting yield surface evolution is shown in Fig. 15.

In addition to an increase in its size, and a translation of its center, the current model clearly predicts a symmetric distortion of the yield surface. In particular, this latter takes the form of an elongation in the direction perpendicular to the current loading direction.

Consider next the case of an orthogonal loading path change from plane-strain tension to simple shear via intermediate unloading corresponding to the discontinuous path shown in Fig. 7. The corresponding evolution of the yield surface is shown in Fig. 16.

During the tension phase (curve TenFin), the yield surface cross hardens as expected in the shear direction. After the shift from tension to shear, the yield surface shrinks continuously in the shear direction (curves TenShe1 to TenShe3) and elongates in the tension direction. This corresponds to cross hardening in the tension direction. Note that the shape of the yield surface at the end of the shear phase approachs that one attained in the monotonic shear test. This is in agreement with the observed experimental behavior for the discontinuous test. The stress state C attained in this case represents the point of maximum possible cross hardening, also in agreement with the experimental discontinuous and path 1 continuous (Figs. 5 and 7) cases. On the other hand, the yield surface development for the continuous loading path 5 predicted by the current model (Fig. 17) shows that the state A reached on this path results in little or no cross hardening. In both cases, the curves TenShe1 represent the yield surfaces predicted by the current model for equal $F_{22} + F_{12}$. Note also the nearly isotropic shape of the yield surface (curve TenShe2) obtained during the transition from shear to tension cross hardening. Since a change in shape of the yield surface is clearly associated with cross hardening here, it is reasonable to regard cross hardening as a special type of distortional hardening, at least in the context of the current model.

Having now examined the model yield surface evolution for LH800, we can take a closer look at the meaning of the values

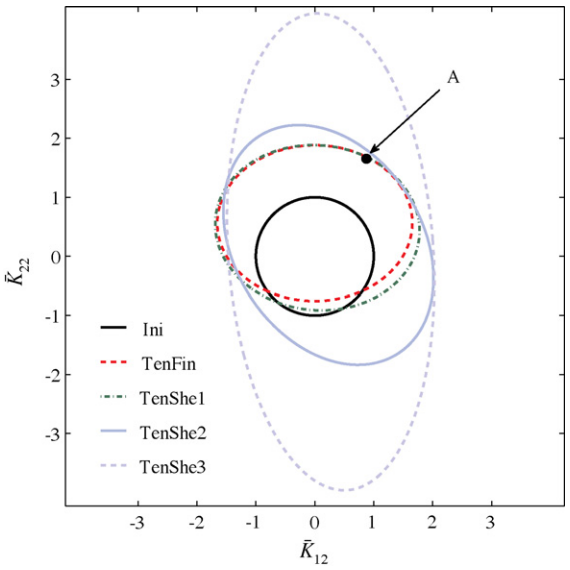

Fig. 17. Predicted yield surface evolution for LH800 during orthogonal loading from plane-strain tension to simple-shear depicted in normalized stress space ($\bar{K}_{12}$, $\bar{K}_{22}$) for the continuous path 5. Ini represents the initial yield surface. TenFin is the final tensile state. TenShe1 to TenShe3 represent subsequent yield surfaces during subsequent loading for the loading path also shown in Fig. 5. The point A indicates the stress state obtained during the experiment and is the same point A as shown in Fig. 8.

obtained for the saturation magnitudes s_d and s_l from Section 4 associated with cross hardening. Since isotropic, kinematic and cross hardening are decoupled in the current model, the special case of pure distortional hardening can be obtained by simply setting s_r and s_x to zero in the identified model. The resulting yield surface development for unixial tension to $F_{22} = 1.2$ and for simple shear to $F_{12} = 0.4$ in the case of pure distortional hardening are shown in Fig. 18.

These are the same deformation paths as in Fig. 15. As expected, pure distortional hardening leads to a pure shape change in the yield surface. This is due in particular to the fact $s_d = 0$ in the fit. In addition, an increase in the yield level in directions orthogonal to the current direction follows for $s_l < 0$. These observations can be used in general with the current model as reasonable constraints on the model identification in order to make this more efficient.

For comparison, consider the yield surfaces obtained by Ishikawa [23] for the steel SUS304 subject to tension and torsion loading as depicted in Fig. 19. For his tests, he used tubes milled from bulk SUS304. After milling, the tubes were annealed, and an average initial yield stress of 194 MPa was obtained using a 50 μm/m definition. The initial yield surface depicted in Fig. 19 was determined with the help of a least-square fit for 12 experimentally determined points on the yield surface. Subsequent yield surfaces were determined by applying a pre-stress. For the tension case depicted in Fig. 19, the experimentally determined Cauchy normal stress σ is 253 MPa, and the corresponding normalized shear stress $\tau_{\mathrm{Nor}} = \sqrt{3}\,\tau$ and the result is -4 MPa. With the help of a model described in earlier work, Ishikawa [23] then determined the centers of subsequent yield surfaces. In the case of torsion to an accumulated inelastic deformation of approximately 10^{-3}, for example, values of 1 MPa for σ and of 284 MPa for τ_{Nor} at the center of the yield surface were obtained in this way. Starting from these, he determined subsequent yield surfaces via radial probing in stress space. As shown in Fig. 19, subsequent yield surfaces determined in this fashion for SUS304 subject to tension and torsion loading are symmetrically distorted. For SUS304, this takes the form of a flattening of the yield surface in the direction of the applied stress. Note that there is neither noticeable isotropic hardening nor cross

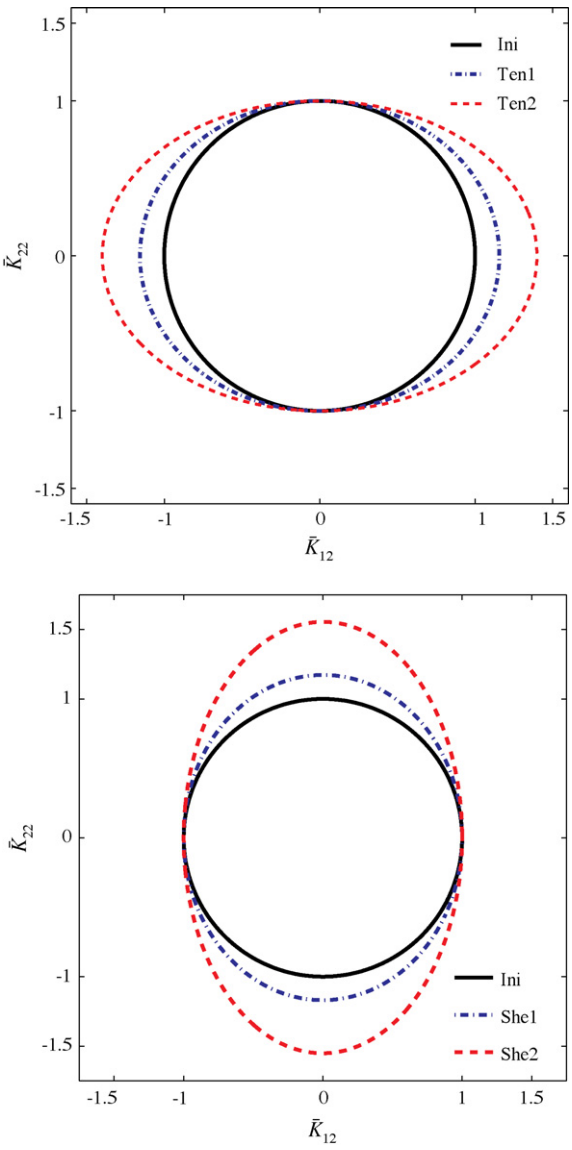

Fig. 18. Yield surfaces development for LH800 during monotonic uniaxial tension (top) and simple shear (bottom) for pure cross hardening. Ini represents the initial yield surface. Ten1 is an intermediate tension stage. Ten2 represents the final tension stage for $F_{22} = 1.2$. She1 is an intermediate shear stage. She2 indicates the yield surface for $F_{12} = 0.4$.

hardening in the sense of an increase in the yield stress in the orthogonal direction for SUS304 at the very small level of pre-strain involved (10^{-3}). This is understandable from the point of view that, at this level of pre-strain, oriented dislocation microstructures responsible for cross hardening have not yet developed. In the case of the IF steel DC06, for example, noticeable cross-hardening occurs only after pre-straining up to approximately 10^{-2}. As the experimental data presented in Section 3 and the above results shows, this is similar for the currently investigated steel LH800.

6. Inelastic state evolution

The previous Section 5 focused on the predictions of the model for stress–strain behavior and yield surface evolution. In this section, attention is directed to the evolution of the internal variables. In contrast to stress–strain relations and the yield surface, internal variables can not be measured experimentally. The interpretation

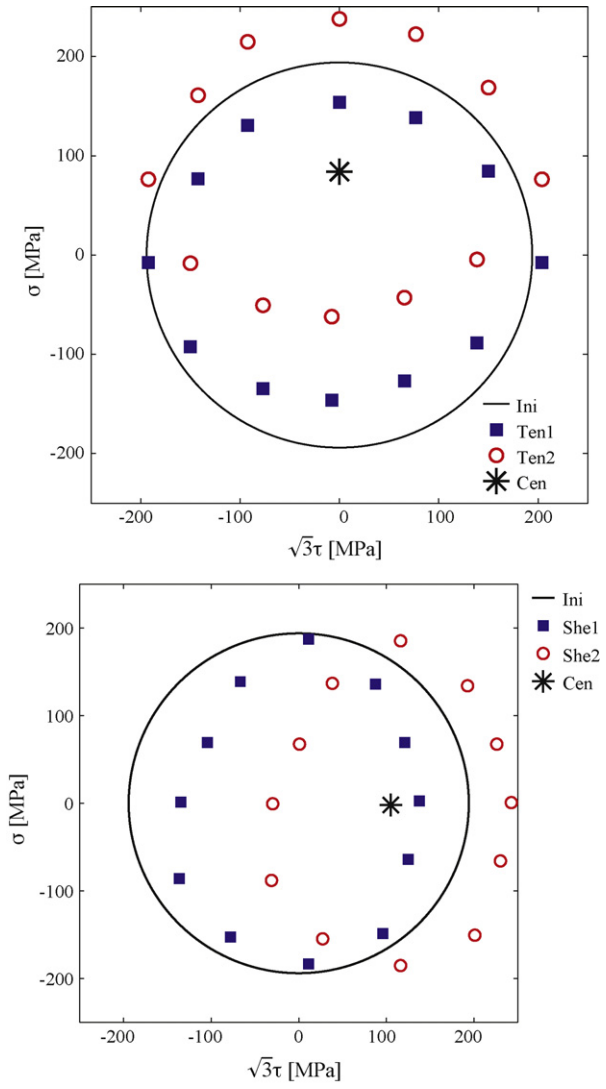

Fig. 19. Yield surfaces after tension (top) and torsion (bottom) obtained by Ishikawa [23] for SUS304. Ini represents the initial isotropic yield surface, Ten1 is the yield surface translated to the origin after tension, Ten2 is the yield surface after tension, She1 and She2 represent the translated and measured yield surfaces, respectively, after torsion. Cen marks the computed center of the subsequent yield surfaces. τ and σ represent the relevant Cauchy shear and normal stresses, respectively.

of the evolution of these in the model context, however, is of interest here.

To begin, consider the development of $\mathcal{A}$. Again, recall that this quantity embodies the effect of oriented dislocation microstructure development on the effective flow anisotropy and yield surface form. Now, as discussed above, along the experimental paths in Fig. 5, the material is subject to first tension in the 2 direction followed by shear in the 1 direction. Since s_d is constrained to be zero, the dominant evolution of $\mathcal{A}$ is in the orthogonal (i.e., shear) direction during the tension phase. Indeed, with $s_d = 0$, (12) can be rewritten in the reduced form

$$\dot{\mathcal{A}} = c_l\, s_l\, (\mathcal{I}_{\text{dev}} - \boldsymbol{N}_{\text{P}} \otimes \boldsymbol{N}_{\text{P}})\, \dot{\alpha}_{\text{P}} - \{c_l\, \mathcal{A} + (c_d - c_l)(\boldsymbol{N}_{\text{P}} \cdot \mathcal{A}\boldsymbol{N}_{\text{P}})\, \boldsymbol{N}_{\text{P}} \otimes \boldsymbol{N}_{\text{P}}\}\, \dot{\alpha}_{\text{P}} \tag{14}$$

in which growth is in the direction $\mathcal{I}_{\text{dev}} - \boldsymbol{N}_{\text{P}} \otimes \boldsymbol{N}_{\text{P}}$ "perpendicular" to $\boldsymbol{N}_{\text{P}} \otimes \boldsymbol{N}_{\text{P}}$. As such, $a_d = \boldsymbol{N}_{\text{P}} \cdot \mathcal{A}\boldsymbol{N}_{\text{P}}$ remains zero during the tension phase, as shown in Fig. 20.

Consequently, $\mathcal{A}_d$ does not influence the yield behavior of the material in the tension phase, but rather only after the orthogonal

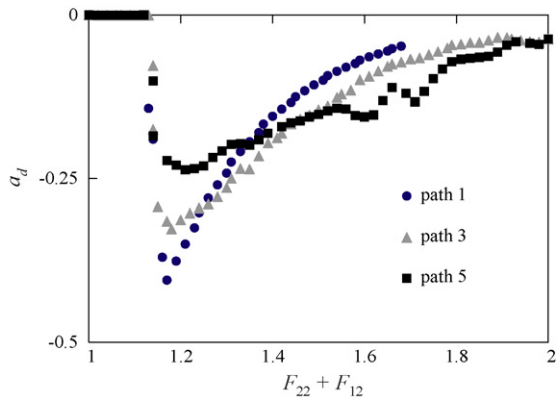

Fig. 20. Evolution of a_d on paths 1, 3 and 5 in Fig. 5. Note that $|\mathcal{A}_d| = |a_d|$.

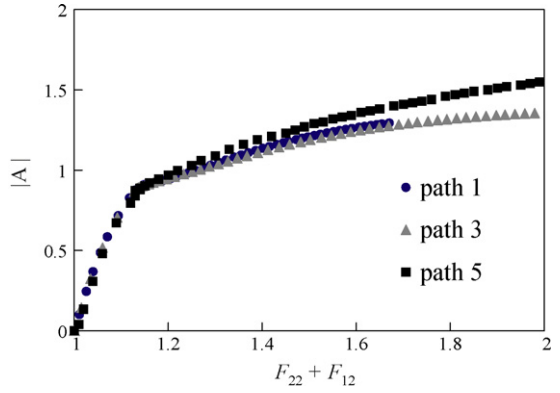

Fig. 21. Development of $|\mathcal{A}|$ on paths 1, 3 and 5 in Fig. 5.

loading direction change into the shear phase. Indeed, as shown in Fig. 20, upon change of loading direction from tension to shear, the projection of $\mathcal{A}$ in the current (i.e., shear) loading direction, i.e., a_d, is now non-zero and negative. Since $s_l < 0$, its magnitude decreases to zero with further loading in the shear direction (Fig. 20). In turn, this results in a contraction of the yield surface in the shear direction. On the other hand, as shown in Fig. 21, $\mathcal{A}$, and so $\mathcal{A}_l$, continue to evolve, resulting in an expansion of the yield surface in the tension direction during the shear loading phase. The amount of cross hardening is inversely correlated with the saturation level for $|\mathcal{A}|$. This correlation can also be established with respect to the development of kinematic hardening. Recall that the form $\sqrt{(\boldsymbol{M} - \boldsymbol{X}) \cdot \mathcal{A}\,(\boldsymbol{M} - \boldsymbol{X})}$ of the equivalent stress measure appearing in the yield condition (8)

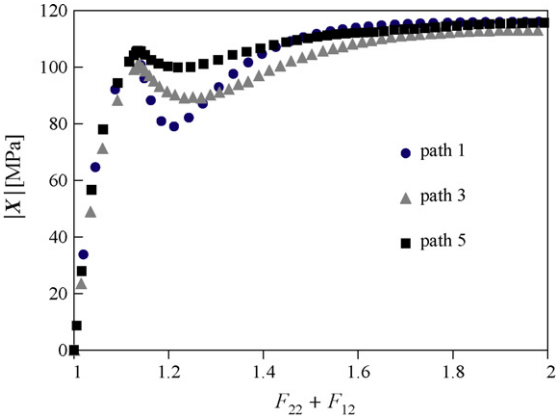

Fig. 22. Evolution of $|\boldsymbol{X}|$ along paths 1, 3 and 5 in Fig. 5.

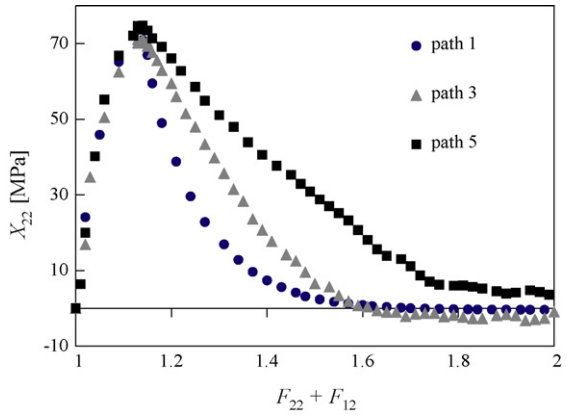

Fig. 23. Development of X_{22} along paths 1, 3 and 5 in Fig. 5.

depends on both $\mathcal{A}$ and $\boldsymbol{X}$. In this sense, these quantities are related to each other, since they both influence the equivalent stress.

Consider next the evolution of the back stress along the paths 1, 3 and 5 in Fig. 5 as displayed in Fig. 22.

As can be seen, $|\boldsymbol{X}|$ increases during the tension stage, decreases at the start of shear stage, and then saturates. Note the nearly perfect correlation of the amount of decrease in $|\boldsymbol{X}|$ with loading path upon change from tension to shear. In particular, the largest decrease occurs along strain path 1, representing the path with the least amount of tension loading. Analogously, the smallest decrease occurs along path 5 having the greatest amount of tension loading. To examine this result in more detail, consider the evolution of the relevant components of $\boldsymbol{X}$. For the tension phase, this is the X_{22}-component, and for the shear phase, the X_{12} component, of $\boldsymbol{X}$. The evolution of the former is shown in Fig. 23.

During the common part of the tension stage, X_{22} develops in basically the same way for all experiments as expected. As exhibited by the results, this changes at the start of the transition from tension to shear. In all cases, X_{22} decreases. The largest decrease occurs in the case of path 1, for which the amount of tension is the smallest. On the other hand, the smallest decrease occurs for path 5 having the largest amount of tension. In all cases, X_{22} decreases basically to zero since the effective saturation value for this component of $\boldsymbol{X}$ goes to zero as $N_{\mathrm{P}22}$ does. As shown by the results in Fig. 24, during the shear phase, the development of X_{12} is the same for all paths, saturating in each case in essence to the monotonic value.

From the point of view of the effective stress and so of the yield surface, then, we see that the decrease of X_{22} during the transition

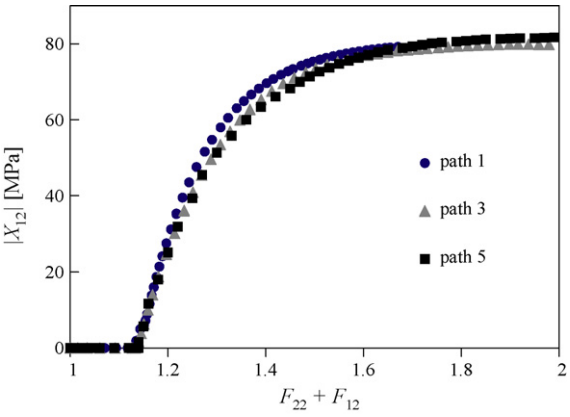

Fig. 24. Evolution of X_{12} along paths 1, 3 and 5 in Fig. 5.

from tension to shear in combination with the development of $\mathcal{A}$ determines to what extent (if at all) a change in form of the yield surface occurs resulting in cross hardening, as shown in Figs. 16–18. In the case of the sharpest drop, i.e., path 1, having the "shortest" tension phase, this change is the largest. On the other hand, for the strain paths 4 and 5, having the longest tension phase, this change is the smallest. As already discussed above in the context of Fig. 11, the superposition of the contributions of r, $\boldsymbol{X}$ and $\mathcal{A}$ is decisive for the modeling of the anisotropic behavior.

7. Summary and conclusions

Motivated by experimental results, a material model for isotropic, kinematic and cross hardening has been formulated, identified and validated for the ferritic steel LH800. The novel aspect of the current approach is the form of the evolution relation for cross hardening, which represents a special type of distortional hardening. This process is modeled with the help of an evolution relation for the fourth-order anisotropic flow tensor $\mathcal{A}$ of the saturation type. As such, this model is a special case of the class of models tacitly introduced by Baltov and Sawczuk [19]. Differences between the current and previous models (e.g., Dafalias et al. [22], Schick [21], Feigenbaum and Dafalias [25]) for the evolution of this tensor include (i) no coupling between kinematic and distortional hardening, and (ii) the form of the evolution relation. As in the current case, the approach of Feigenbaum and Dafalias [26] involves no coupling of the evolution of the back stress and $\mathcal{A}_{\mathrm{Bal}}$. The focus in their case is on the asymmetric development of the yield surface rather than on the effect of cross hardening as in the current work. In contrast to all previous models, the form of the evolution relation for $\mathcal{A}$ is determined by the split of $\mathcal{A}$ into parts parallel $\mathcal{A}_d$ and perpendicular $\mathcal{A}_l$ to the current loading direction in stress space. This split is physically motivated with the help of TEM investigations of the development of oriented dislocation microstructures (e.g., Nesterova et al. [29]) directly related to the history of the loading path direction and its changes. The form of the evolution relation for $\mathcal{A}$ is formally analogous to that introduced by Wang et al. [15] as based on the earlier work of Teodosiu and Hu [2] for the fourth-order hardening tensor $\mathcal{S}$ whose evolution accounts for the effect of cross hardening on the flow behavior. In contrast to the class of models based on the approach of Baltov and Sawczuk [19], this tensor affects the current yield stress level rather than the effective stress level. As such, there is no change of shape of the yield surface associated with cross hardening in the class of models based on Teodosiu and Hu [2], Wang et al. [15]. Unlike the Teodosiu and Hu [2] model, the current model does not account for additional effects like hardening stagnation after load reversal. In work in progress, a more detailed comparison of the two classes of models is being carried out. In addition, a thermodynamically consistent framework for the current model analogous to that of Schick [21], Feigenbaum and Dafalias [25] represents on-going research and will be reported on in future work.

Acknowledgments

We thank the reviewers of a previous version of this work for their very helpful comments which have lead to significant improvement. Partial financial support for this work provided by the German Science Foundation (DFG) under contract SPP 1204/2 is greatly acknowledged.

References

[1] C. Teodosiu, Z. Hu, S.F. Shen, P.R. Dawson, Simulation of Materials Processing: Theory, Methods and Applications, Balkema, Rotterdam, 1995, pp. 173–182.

[2] C. Teodosiu, Z. Hu, Proceedings of 19th Risø International Symposium on Material's Science: Modelling of Structure and Mechanics of Materials from Microscale to Product, Risø National Laboratory, Roskilde, Denmark, 1998, pp. 149–168.
[3] S. Hiwatashi, A. Van Bael, P. Van Houtte, C. Teodosiu, Comput. Mater. Sci. 9 (1997) 274–284.
[4] S. Hiwatashi, A. Van Bael, P. Van Houtte, C. Teodosiu, Int. J. Plast. 14 (1998) 647–669.
[5] T. Hoc, S. Forest, Int. J. Plast. 17 (2001) 65–85.
[6] B. Peeters, M. Seefeldt, C. Teodosiu, S.R. Kalidindi, P. Van Houtte, E. Aernoudt, Acta Mater. 49 (2001) 1607–1619.
[7] B. Peeters, B. Bacroix, C. Teodosiu, P. Van Houtte, E. Aernoudt, Acta Mater. 49 (2001) 1621–1632.
[8] B. Peeters, S.R. Kalidindi, C. Teodosiu, P. Van Houtte, E. Aernoudt, J. Mech. Phys. Solids 50 (2002) 783–807.
[9] F. Barlat, J. Brem, J. Yoon, K. Chung, R. Dick, D. Lege, F. Pourboghrat, S.H. Choi, E. Chu, Int. J. Plast. 19 (2003) 1297–1319.
[10] S. Li, E. Hoferlin, A. Van Bael, P. Van Houtte, C. Teodosiu, Int. J. Plast. 19 (2003) 647–674.
[11] S. Bouvier, C. Teodosiu, H. Haddadi, V. Tabacaru, J. Phys. IV France 105 (2003) 215–222.
[12] S. Bouvier, J. Alves, M. Oliveira, L. Menezes, Comput. Mater. Sci. 32 (2005) 301–315.
[13] S. Bouvier, B. Gardey, H. Haddadi, C. Teodosiu, J. Mater. Process. Technol. 174 (2006) 115–126.
[14] H. Aretz, Int. J. Plast. 24 (2008) 1457–1480.
[15] J. Wang, V. Levkovitch, F. Reusch, B. Svendsen, J. Hu'etink, M. van Riel, Int. J. Plast. 24 (2008) 1039–1070.
[16] M. van Riel, A.H. van den Boogaard, Scr. Mater. 57 (2007) 381–384.
[17] R. Hill, The Mathematical Theory of Plasticity, Oxford Classic Texts in the Physical Sciences, Oxford University Press, 1950.
[18] M.C. Oliveira, J.L. Alves, B.M. Chaparro, L.F. Menezes, Int. J. Plast. 23 (2007) 516–543.
[19] A. Baltov, A. Sawczuk, Acta Mech. I (1965) 81–92.
[20] G.Z. Voyiadjis, M. Foroozesh, J. Appl. Mech. 57 (1990) 537–547.
[21] D. Schick, Anisotropic Plasticity and Viscoplasticity, Ph.D. thesis, TU Darmstadt, 2004.
[22] Y. Dafalias, D. Schick, C. Tsakmakis, Deformation and Failure in Metallic Materials (Lecture Notes in Applied and Computational Mechanics), Springer, Berlin, 2003.
[23] H. Ishikawa, Int. J. Plast. 13 (1997) 533–549.
[24] M. Yeganeh, Int. J. Plast. 23 (2007) 2029–2057.
[25] H.P. Feigenbaum, Y.F. Dafalias, Int. J. Solids Struct. 44 (22–23) (2007) 7526–7542.
[26] H.P. Feigenbaum, Y.F. Dafalias, J. Eng. Mech. 134 (2008) 730–738.
[27] A. Phillips, J.L. Tang, M. Ricciuti, Acta Mech. 20 (1974) 23–39.
[28] M. Boucher, J.P. Cordebois, Int. J. Plast. 10 (1994) 909–933.
[29] E.V. Nesterova, B. Bacroix, C. Teodosiu, Mater. Sci. Eng. A309–A310 (2001) 495–499.
[30] A.E. Tekkaya, A. Brosius, T. Cwiekala, F.-W. Bach, O. Grydin, M. Schaper, B. Svendsen, C. Barthel, MEFORM 2008—Simulation von Umformprozessen, Freiberg, Germany, 2008, pp. 262–274.
[31] J.C. Simo, T.J.R. Hughes, Computational Inelasticity, Springer Verlag, 1998.
[32] B. Svendsen, Int. J. Solids Struct. 38 (2001) 9579–9599.
[33] N. Stander, W. Roux, T. Goel, T. Eggleston, K. Craig, LS-OPT Users Manual, Livermore Software Technology Corporation, 2008.
[34] H. Haddadi, S. Bouvier, M. Banu, C. Maier, C. Teodosiu, Int. J. Plast. 22 (2006) 2226–2271.
[35] P. Flores, L. Duchene, C. Bouffioux, T. Lelotte, C. Henrard, N. Pernin, A. Van Bael, S. He, J. Duflou, A.M. Habraken, Int. J. Plast. 23 (2007) 420–449.